CERN/SPSC 97-11
SPSC / I214
May 8, 1997

Letter of Intent submitted to the
27-28 May 1997 meeting
of the CERN SPSC

Near Threshold Baryon/Anti-Baryon Production in pp Collisions

L.C. Bland,[a,b] W. Eyrich,[d] D. Filges,[b] R. Geyer,[b] D.R. Gill,[g] D. Grzonka,[b] W.W. Jacobs,[a]
L. Jarczyk,[c] T. Johansson,[e] A. Khoukaz,[f] K. Kilian,[b] S. Kistryn,[c] A. Magiera,[c] R. Maier,[b]
P. Moskal,[c] H. Nann,[a,b] W. Oelert,[b] E. Roderburg,[b] R. Santo,[f] T. Sefzik,[b] J. Smyrski,[c]
G. Sterzenbach,[b] F. Stinzing,[d] A. Strzalkowki,[c] S.E. Vigdor,[a] St. Wirth[d] and P. Zolnierczuk[c]

[a] *Indiana University Cyclotron Facility, Bloomington, IN USA*
[b] *Institut für Kernphysik, Jülich GERMANY*
[c] *Institute of Physics, Jagellonian University, Cracow POLAND*
[d] *Physikalisches Institut, Universität Erlangen, Erlangen GERMANY*
[e] *Uppsala University, Uppsala SWEDEN*
[f] *Institut für Kernphysik, Universität Münster, Münster GERMANY*
[g] *TRIUMF, Vancouver CANADA*

I. Introduction

The LEAR program was extremely successful at providing accurate cross sections and polarization observables for low-energy, antiproton-induced reactions. LEAR was a unique facility for the study of $p\bar{p}$ elastic scattering; $p\bar{p} \rightarrow n\bar{n}$ charge-exchange, from PS-199; and strangeness-producing reactions, such as $p\bar{p} \rightarrow \Lambda\bar{\Lambda}$, from PS-185. These data have yielded important insights into particle/anti-particle strong-interaction dynamics. They still hold the promise of revealing an explicit role of non-perturbative quark and gluon dynamics [1] in addition to the more conventional descriptions involving meson-exchange forces.

Concurrent with the LEAR program have been extensive studies of heavy-ion reactions at many laboratories, with the goal of studying the nuclear equation of state and searching for phase transitions of nuclear matter at high temperature and/or pressure. One of the many challenges of such studies is to provide a sufficiently complete microscopic description of the many possible reactions to establish whether the interpretation of experimental signatures require the introduction of new phenomena (such as phase transitions) or can be described by more conventional reaction dynamics. Fully microscopic descriptions of these complex reactions are not possible. One of the reasons for this is a lack of information of elementary meson production or baryon/anti-baryon production reactions.

This letter of intent proposes a new experiment for the CERN-PS east hall that would provide data that can serve as a 'bridge' between the LEAR program and heavy-ion physics. We propose to measure cross sections for proton-induced baryon/anti-baryon production reactions near the kinematic thresholds; *i.e.*, $pp \rightarrow ppB\bar{B}$, with $B\bar{B}$ representing either a proton/anti-proton, neutron/anti-neutron or hyperon/anti-hyperon pair. Analogous to the LEAR program, these reactions probe the fundamental process of the conversion of energy into strongly-interacting matter. As a step towards complex heavy-ion collisions producing antibaryons, the $pp \rightarrow ppB\bar{B}$ reaction produces $B\bar{B}$ pairs in a system with net baryon number equal to two. This is in contrast to the LEAR studies of $p\bar{p} \rightarrow B\bar{B}$ reactions which have net baryon number zero. As described in more detail below, no data exist for the elementary $pp \rightarrow pp(p\bar{p})$ production reaction below the threshold where additional pions are also produced. The experiment described in this letter would provide the first measurements of this type.

II. Theoretical motivation

The experimental programs at the IUCF Cooler ring, CELSIUS at Uppsala and COSY at Jülich have principally focused on near-threshold meson production in pp collisions, including π, η, ω and mesons with valence strange quarks (ϕ and K^+K^- pairs). Data from these reactions have clearly illustrated the role played by short-range strong interactions [2], the influence of baryon resonances and the contributions of multi-step processes [3]. $B\bar{B}$ pair creation in pp collisions is intimately related to the dynamics of meson production. Within a quark based picture, this process is necessarily higher twist since the quarks and anti-quarks boosted onto the mass shell from the QCD sea must be correlated to produce the $B\bar{B}$ pair observed in the final state. Intercomparisons of $p\bar{p}$, $n\bar{n}$ and $\Lambda\bar{\Lambda}$ production can provide complementary knowledge of the $u\bar{u}$, $d\bar{d}$ and $s\bar{s}$ content of the quark sea to that obtained from meson production. Within a meson-exchange picture, $p\bar{p}$ and $n\bar{n}$ production are predicted to be dominated by vector mesons [4]. Hence, an intercomparison of their production can separately illuminate the role played by ρ and ω mesons. To experimentally ascertain the quantum state of the produced $B\bar{B}$ pair requires additional polarization measurements that could be made at a future hadron facility such as LISS [5]. Finally, very little data exists for the elementary $p\bar{p}$ production process, particularly below the incident energy where additional mesons are produced, thereby hindering the understanding of $p\bar{p}$ production in heavy-ion collisions [4].

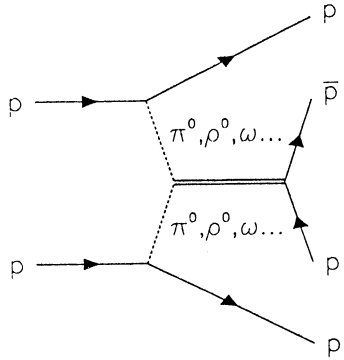

Figure II.1 The diagram corresponding to the OBE calculation of the $pp \rightarrow pp(p\bar{p})$ reaction [4].

A microscopic calculation of the $pp \rightarrow pp(p\bar{p})$ reaction within the framework of a one-boson exchange model has recently been carried out. The goal of that work was to deduce a theoretical amplitude for the elementary process to be used for understanding data from heavy-ion collisions. The authors consider a diagram for the process as shown in Fig. II.1, equivalent to the off-shell production of π,ρ and ω pairs in pp collisions that annihilate to form the final-state $p\bar{p}$ pair. In their calculation, the $pp\pi^0(\rho,\omega)$ vertices are treated by a one-boson exchange (OBE) model, with parameters consistent with nucleon-nucleon scattering. The $\pi\pi$ ($\rho\rho$) $\rightarrow p\bar{p}$ amplitudes are taken from measured $p\bar{p}$ annihilation data, with an assumed t dependence to extrapolate the measured amplitudes off the mass shell. The $\omega\omega \rightarrow p\bar{p}$ amplitudes are assumed the same as for $\rho\rho \rightarrow p\bar{p}$ since no data exist for that $p\bar{p}$ annihilation channel. The authors have not included in their calculation either final-state interactions (FSI) or effects from the necessary anti-symmetrization of the three protons in the final state. Instead they argue that they expect modifications only very close to the kinematic threshold, since enhancements from FSI in $pp \rightarrow pp\eta$ are restricted to values of $\varepsilon \equiv \sqrt{s} - 4m_p \leq 40$ MeV.

The results of the OBE calculation for the $pp \rightarrow pp(p\bar{p})$ reaction are shown in Fig. II.2. The data in that figure are from inclusive $\bar{p}$ production at much higher energies [6]. That data agrees well with the predictions of the LUND string model [7]. Previously, in the analysis of subthreshold $\bar{p}$ production in heavy-ion collisions, a logarithmic extrapolation of the higher

energy data had been employed. The new calculation results in more than an order of magnitude smaller cross section near threshold than this simple extrapolation.

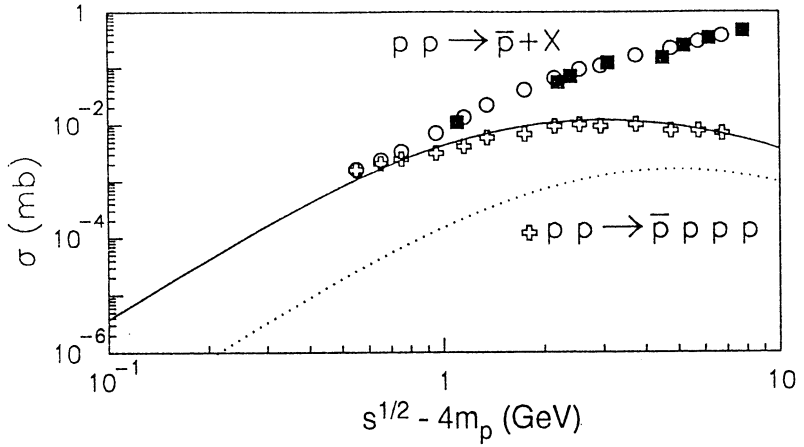

Figure II.2 The antiproton total cross section as a function of the invariant energy above threshold from Ref. [4]. The full squares are data for inclusive production [6]. The open circles are calculations of the antiproton production within the LUND string model [7]. The crosses represent the LUND model predictions for the exclusive $pp \rightarrow pp(p\bar{p})$ channel. The solid line is the OBE model calculation [4] including π^0, ρ and ω exchange. The dotted line is the π^0 exchange contribution only.

There are several things to note about the OBE model calculation of the $pp \rightarrow pp(p\bar{p})$ reaction.

- The authors predict a total cross section of approximately 1 nb for the reaction at $\varepsilon \equiv \sqrt{s} - 4m_p \sim 50$ MeV.
- The energy dependence of the total cross section is dominated by phase space.
- The ρ and ω exchange contributions are predicted to be more than an order of magnitude larger than for π^0 exchange, illustrating the sensitivity of the reaction to the short-range nucleon-nucleon interaction.

A natural question to ask is what range of $\varepsilon \equiv \sqrt{s} - 4m_p$ *should be probed in an experiment studying the* $pp \rightarrow pp(p\bar{p})$ *reaction*? This choice will dramatically influence the detector design, background contributions and nearly all other aspects of the experiment.

- Experimental considerations (primarily the size of the cross section) will set the lowest value of ε that can be probed.
- The maximum ε to be probed can be decided based on the influence of *final state interactions* (FSI).
- A minimum of three values of ε are required to establish the energy dependence of the total cross section.

Since the final state in the production of $B\bar{B}$ pairs in pp collisions contains four strongly interacting particles, the dynamics of the production process are significantly influenced by FSI. It is likely that the near-threshold cross section will be enhanced because of them. A competing effect for the $pp(p\bar{p})$ final state is that the Pauli principle forbids three protons from all having relative angular momentum equal zero, thereby decreasing the

threshold cross section. A sufficient range of ε is required to separate the more interesting short-range strong interaction dynamics from these more trivial effects. Hence, the upper limit for ε must be chosen so as to minimize the influence of FSI.

In Fig. II.3*(a)*, the solid line shows the fraction of phase space as a function of ε having all pairs of protons with relative energy > 2 MeV. For smaller relative energies, proton pairs undergo strong final state interactions, specified by the Watson-Migdal distribution. The dashed line in this figure is that fraction of phase space where *all* pairs of particles in the

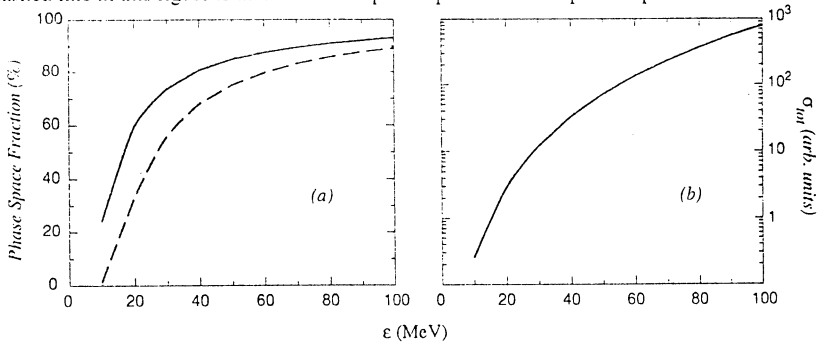

Figure II.3 *(a)* Phase space fractions (defined in the text) vs. ε *(b)* Variation of the total cross section for the $pp(p\bar{p})$ final state with energy, as expected for pure phase space.

$pp(p\bar{p})$ final state have relative energies in excess of 2 MeV. Both curves begin to plateau at a CM total kinetic energy, $\varepsilon \sim 50$ MeV suggesting this as a natural upper limit for the experiment. Fig. II.3*(b)* shows the predicted ε dependence of the total cross section, assuming pure phase space. It is likely that the competing effects of FSI and the Pauli exclusion principle will severely distort this energy dependence.

III. Summary of experiment

Based on the experience gained in the study of meson production reactions near kinematic thresholds at low-energy, stored beam facilities (close 'cousins' to LEAR), it is in principle quite simple to study the threshold production of $B\bar{B}$ *pairs using proton beams extracted from the CERN PS. As in meson production near threshold, there are* ***severe kinematic constraints*** *that limit the size of an apparatus that subtends the full reaction phase space and serve to provide powerful discrimination between signal and background.* Some relevant thresholds are shown in Table 1.

Table 1 Examples of proton-induced reaction thresholds

Reaction	p_{beam} at threshold (GeV/c)
$pp \rightarrow pp\pi^0$	0.777
$pp \rightarrow pp\eta$	1.986
$pp \rightarrow pK^+\Lambda$	2.339
$pp \rightarrow ppK^+K^-$	3.302
$pp \rightarrow pp(p\bar{p})$	6.501
$pp \rightarrow pp(\Lambda\bar{\Lambda})$	7.999

III.A Kinematic considerations

For the study of $p\bar{p}$ pairs produced in pp reactions close to threshold, we require a proton beam with

- momentum, $p_{beam} \geq 6.5$ GeV/c;
- small momentum spread, $\Delta p/p \leq 10^{-4}$;
- emittance less than 1 π mm-mr.

Proton beams from the CERN PS are ideally suited to these requirements. For illustrative purposes, if we consider the situation where the total available kinetic energy in the center of mass for the $pp(p\bar{p})$ final state is $\varepsilon = \sqrt{s} - 4m_p = 10$ MeV, then we find that all outgoing particles stay within a small cone of half-angle, $\vartheta = 15$ mr, and have a maximum momentum spread of ±15% around an average momentum equal to one-fourth that of the beam. The kinematic constraints imposed by studying the reaction near threshold imply that a modestly sized dipole spectrometer can be used to momentum analyze the reaction products, but still yield 100% phase space acceptance for all four outgoing particles.

III.B Experimental approach

Below, we provide a *qualitative description of the experimental requirements* for the study of the $pp \rightarrow pp(p\bar{p})$ reaction near the kinematic threshold. The specific kinematics considered here are for $\varepsilon = 25$ MeV. Results from a more quantitative study of this reaction are presented in section IV.

The experiment will consist of a ~6 cm long liquid hydrogen target positioned upstream of a large-gap dipole magnet approximately 1 m in length with a field strength of approximately 1 T, as shown in Fig. III.1. Such a magnet would bend the primary beam by 50 mr, the reaction protons by 200±85 mr and the reaction antiprotons by -200±85 mr. Hence, all of the reaction particles are contained within small, approximately conically shaped volumes after being momentum analyzed by the magnet and are fully separated from the unscattered beam protons. In order to reconstruct the momentum vectors of the four reaction products, we need tracking detectors on both sides of the magnet. Track measurements can be performed, for example, with two packages of straw-tube detector stacks having rough dimensions of 0.8 m (horizontal) × 0.5 m (vertical) positioned downstream of the magnet and a sufficient thickness to sample enough points to reconstruct the track. Following the tracking detectors, a scintillator hodoscope, having both vertical and horizontal slabs, is necessary for event triggering and energy-loss and time-of-flight measurements.

A vacuum system would enclose the hydrogen target and extend to the tracking detectors. Both beam and reaction particles are transported through the vacuum system, thereby minimizing the probability of unwanted secondary reactions. This configuration ensures that the backgrounds produced by the apparatus are small. The remaining backgrounds are from other reactions in the target; most dominantly, multiple pion production reactions, $pp \rightarrow pp(n\pi)$. The severe kinematic constraints ensure that a trigger which selects 3 positive particles on one side of the magnet and 1 negative particle on the other side produces small rates from these background processes, so long as the scintillator hodoscope subtends only the cones expected for the $pp(p\bar{p})$ final state. As demonstrated in the following section, the kinematic constraints imposed by the study of the threshold reaction suggest that offline event reconstructions can produce a clean signature even if the total cross section for the reaction is only 10^{-8} of the total pp cross section.

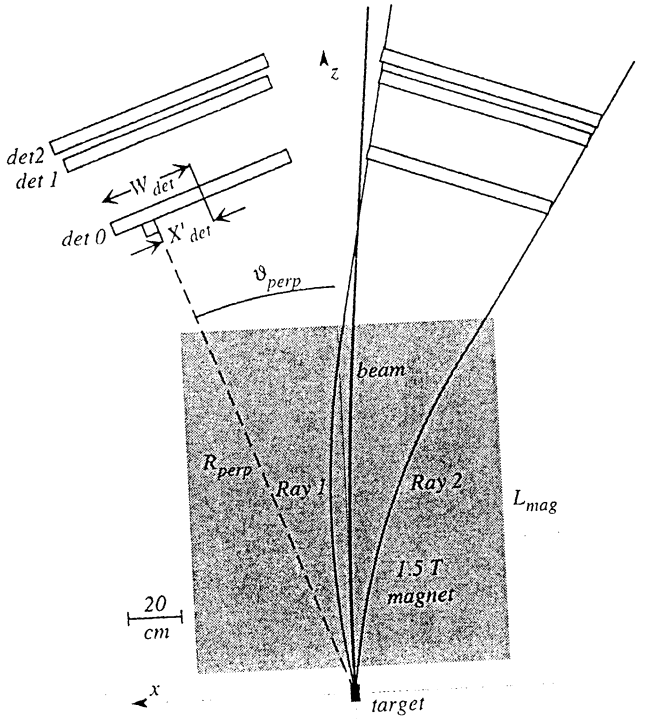

Figure III.1 Simple detector arrangement for study of the $pp(p\bar{p})$ final state near threshold. The limiting rays (1 and 2) determine the transverse extent of the detector apparatus and are defined in the text.

III.C Cross sections and rates

There are no cross section data in the threshold region for the process $pp \rightarrow \bar{p}X$. As discussed in section II, theoretical estimates predict a total cross section of ~1 nb at ε~50 MeV. With a beam of 1.2×10^8 protons per spill and a spill every 1.2 s, we obtain an average beam intensity of 10^8 protons/sec and an instantaneous intensity of 4×10^8 protons/sec, for a 0.3 sec long spill. Using a 6 cm long liquid hydrogen target, there is a 1% reaction probability (corresponding to $\sigma_{tot} = 40$ mb for pp scattering) implying an average reaction rate of 1 MHz (and an instantaneous reaction rate of 4 MHz). *For a total cross section for the* $pp \rightarrow pp(p\bar{p})$ *reaction of 1 nb, we get 2.5* $\times 10^{-2}$ *reactions of interest per second, or 170 per day, assuming an overall efficiency of 80% for data collection and beam availability of 1 spill out of every 10.*

IV. Monte-Carlo simulations

Although the qualitative advantages of performing a measurement of the $pp \to pp(p\bar{p})$ reaction near the kinematic threshold are obvious, there still remain quantitative questions about the size of the magnet necessary to do the measurements, the approach used for event reconstruction and the ability to distinguish the desired signal in the presence of prolific background processes (which are *8 orders of magnitude* more probable). To address these questions, it is necessary to resort to simulation methods of the $pp \to pp(p\bar{p})$ process itself and of the most dominant background processes. Events generated by the simulations are then reconstructed to establish the performance of the detector apparatus and the feasibility of the experiment. This section describes the simulation approach, the event reconstruction and the results from the simulation study.

IV.A Kinematic limits and detector acceptance

To establish the necessary dimensions of the magnet and tracking detectors, the kinematical limits for the reaction need to be examined. The suitability of such a simple setup can be established by considering whether the kinematical constraints associated with a threshold reaction are sufficient to distinguish signal from background, and if not, what additional apparatus is required to make that distinction. The overall scale of the detection apparatus is dictated by the highest energy above threshold that will be probed in the experiment. The geometry of the experiment is specified by the magnet length (L_{mag}) and detector positions (given by the perpendicular distance from the target, R_{perp}; the rotation angle, ϑ_{perp}; and the shift, X_{det}) and sizes (given by the in-plane and out-of-plane half-extents, W_{det} and H_{det}). These quantities are defined in Fig. III-1. For the simulation studies presented below a magnet of length, L_{mag}=1.3 m, a central field strength of 1.5 T and a usable gap between the poletips of 0.5 m was used. The detector dimensions, giving full acceptance for $\varepsilon \leq 50$ MeV, that were used in the simulations are listed in Table 2.

Table 2 Detector dimensions. See Fig. III.1 and the text for the definition of the quantities.

Quantity	det 0	det 1	det 2
R_{perp} (cm)	156	185	189
ϑ_{perp}	±20°	±20°	±20°
X_{det} (cm)	-15	-20	-20
W_{det} (cm)	45	55	60
H_{det} (cm)	30	40	45
element width (cm)	*	*	3.0

* Value not specified in simulation/reconstruction

These detector dimensions have been optimized for the magnet used. As discussed below, a smaller magnet could be used for the experiment at the expense of longer distances and larger transverse areas for the detectors. A final decision about the setup should be made only after a suitable magnet is located.

IV.A.1 Kinematic limits

Much can be learned about the reaction under consideration by analytic calculations of the kinematics of the process. In particular, the limiting angles and the particle momenta for a given value of $\varepsilon \equiv \sqrt{s} - 4m_p$ are determined from the kinematic relations

$$\sin\vartheta_{max} = \frac{\beta^*_{max}\gamma^*_{max}}{\beta_{CM}\gamma_{CM}}$$

$$p_{max(min)} = \gamma_{CM}\left(\pm p^*_{max} + \beta_{CM}E^*_{max}\right)$$

where E^*_{max} is the maximum proton energy in the CM for the $pp(p\bar{p})$ final state;

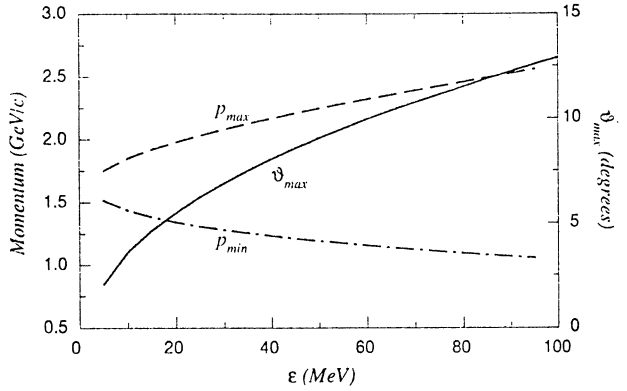

Figure IV.1 ϑ_{max} and $p_{max(min)}$ vs. ε for the $pp(p\bar{p})$ final state.

$\beta^*_{max}\gamma^*_{max} = p^*_{max}/m_p$; ϑ_{max} is the maximum laboratory frame polar angle; and the limiting laboratory frame momenta are given by $p_{max(min)}$. Fig. IV.1 shows the functional dependence of ϑ_{max} and $p_{max(min)}$ on ε.

IV.A.2 Event distributions on detectors

Given the choice of ε_{max}=50 MeV, it is now necessary to choose the magnet geometry and detector dimensions required to separate the reaction products from the beam and to give 100% acceptance for the $pp(p\bar{p})$ final state. To ensure this, it is necessary that the proton limiting ray have an exit angle from the magnet which is larger than the beam deflection angle. The limiting ray (labeled *Ray 1* in Fig. III.1) corresponds to the proton simultaneously having maximum values for its in-plane momentum and in-plane scattering angle. This is equivalent to the proton having its maximum possible momentum at an angle of 90° in the CM frame, or

$$p_x = p^*_{max} \text{ and } p_z = \beta_{CM}\gamma_{CM}E^*_{max}\text{, where}$$

$$\beta_{CM} = \frac{p_{beam}}{E_{beam} + m_{targ}}$$

$$E^*_{max} = \frac{s - 8m_p^2}{2\sqrt{s}}$$

The resulting angle difference between the beam and the limiting ray is shown in Fig. IV.2 as a function of $B\rho$. As is evident, even a moderate sized magnet provides separation between the beam and the reaction products. For the purposes of the simulation, a 1.3-m long magnet has been used. This is comparable in size to the PS-170 magnet presently in use for experiment LNS-E213 at Laboratoire National Saturne for ongoing $\vec{p}p \to pK^+\vec{\Lambda}$ and $\vec{p}p \to pp\phi$ measurements [8] and scheduled to be returned to CERN. A final decision about the detector geometry can only be made once a suitable magnet has been located.

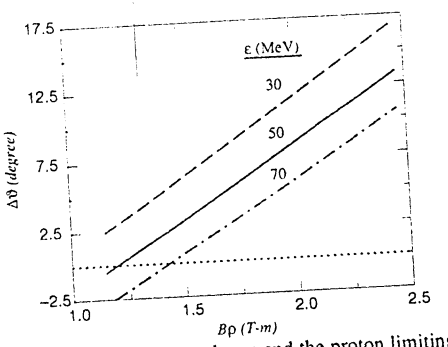

Figure IV.2 Angle difference between beam and the proton limiting ray at the exit from the magnet for the $pp(p\bar{p})$ final state. To fully separate the positive reaction products from the beam, $\Delta\vartheta$ must be greater than 0.

The distribution of hits on the detector system (Fig. IV.3) can be determined from analytic means and also via Monte-Carlo (described below). For a given CM angle, ϑ_{CM}, there is a bounding locus of events in a plane lying along each detector. All protons from the $pp(p\bar{p})$ final state must fall within this locus, the exact location depending on the magnitude of momentum in the CM, $p^* \le p^*_{max}$, and the direction of the transverse momentum. The shape

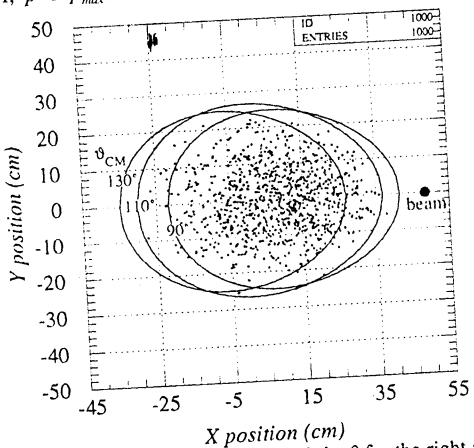

Figure IV.3 Distribution of events on the face of *det 0* for the right arm. The point X=Y=0 is at the mid-point of the detector used in the simulations. Also shown are the kinematic limits for the $pp(p\bar{p})$ final state and the beam position at ε=50 MeV.

of the loci depends on the strength of the magnetic field and the orientation and placement of the detectors. The detector geometry necessary to obtain full acceptance for $\varepsilon \le 50$ MeV is given in Table 2.

IV.B Simulation procedure

Quantitative questions about the feasibility of the experiment (such as the track reconstruction resolution, separation of the $pp(p\bar{p})$ signal from background, *etc.*) require a detailed Monte Carlo. In principle, GEANT provides all of the necessary tools to examine the $pp(p\bar{p})$ final state and potential background reactions. In practice, GEANT generates events at a rate of only ~4 Hz. Hence, it is not feasible to generate the many background events necessary to establish what satisfies the experiment trigger. Instead, the GEANT phase-space generator (GENBOD) was used as the starting point for an independent simulation that relied on analytic calculations of the helical trajectory of the charged particles in a constant magnetic field. The intercepts of the charged particles with a flexibly specified detector system and the imposition of a realistic trigger were performed for each event. Missing from this simulation were multiple scattering, particle decays and interactions and a realistic treatment of the fall off of the magnetic field at the edge of the magnet. Nonetheless, the simulation program operated at ~2 kHz making it feasible to explore the influence of the trigger on background reactions and ultimately provided a set of momentum 4-vectors that were used in the full GEANT simulation which included all of these effects. A brief description of the ingredients of the simulation is provided below.

IV.B.1 Coordinate system and magnetic field specification

The coordinate system used for both simulations and the event reconstruction has the *z*-axis along the incident beam direction (far away from the magnetic field), the *y*-axis oriented vertically upward and the *x*-axis pointing to beam left. The beam is assumed to be deflected to negative *x* when passing through the magnet, hence the central magnetic field has $B_y>0$ and $B_x \approx B_z \approx 0$, except near the poletipes of the magnet where the fringe fields are large

The 'analytic' simulations have been performed with a 'sharp cutoff' magnetic field, meaning that the field is assumed to be constant, $B_y=B_{cent}$ inside of the effective field boundary and zero outside. The influence of fringe fields and magnetic field non-uniformities are expected to be a second order effect, not effecting the primary conclusions. To check this assumption, a model of a real magnetic field, including fringe field effects [9], has been used in a GEANT-based simulation. In this model, the fringe field of a dipole magnet of gap width *D* depends on a profile function, $h(s)$, given by the ratio of the magnetic field in the median plane to the central field strength, B_0, by:

$$h(s) = \frac{B_y(0,0,z)}{B_0} \cong \frac{1}{1+e^S}\ , \quad \text{where } S = \sum_{n=0} c_n s^n \ \text{ and } s = \frac{z}{D}$$

Within this model, the fringe field is given by

$$B_y(0,y,z) = B_0\left[h(s) - \frac{y^2}{2D^2}\frac{d^2h}{ds^2}\right]$$

$$B_z(0,y,z) = \frac{y}{D}B_0\frac{dh}{ds}$$

IV.B.2 Detector specification

Two types of detectors are allowed for in the simulations. In the first type, the detector is assumed to be able to return the simulated coordinates of a charged-particle track crossing with some finite resolution. That resolution is represented by picking transverse coordinate measurement errors (δx and δy) at random from Gaussian distributions having an input σ_x and

σ_y. Hence, the important effects from single detector channels sharing hits from multiple charged-particle track crossings are not included. Furthermore, the event reconstructions presented below do not include hit matching errors, probably the dominant source of systematic errors for the track fitting. It is assumed that either multi-wire drift chambers (MWDC) or straw-tube detectors will be used for tracking. Hence, σ_x=σ_y=100 μm has been used in the calculations.

The second type of detector includes multiple planes and finite element widths. For these detectors, the track crossing coordinates are 'digitized' to identify the hit detector elements. This allows for the total number of hit elements to be determined for each event. A realistic treatment of event triggering for both the $pp(p\bar{p})$ final state and background processes (discussed below) is then possible.

IV.B.3 Event generation and particle transport

The CERNLIB routine, GENBOD, is used to generate events picked uniformly from n-body phase space. To represent the rapid energy dependence of the $B\bar{B}$ production and to provide a more realistic ratio of background processes such as $pp \rightarrow pp\pi^+\pi^-(m\pi)$ for different values of m, Fermi energy dependence is used.

The finite target length is included in the calculations by drawing events uniformly distributed along a 6-cm target length.

The helical path followed by the charged particles in the magnetic field volume is computed analytically given momentum components parallel and perpendicular to the uniform field. Multiple Coulomb scattering is not included in the calculations.

Unstable particles can be treated. A secondary vertex is drawn at random from an exponential distribution, $e^{-d/\beta\gamma\tau}$, where τ is the particle lifetime and d is the distance from the primary vertex to the decay of the unstable particle. The resulting secondary particles are tracked through the magnetic field.

IV.C Event triggering and background reactions

The trigger system is required to reduce the rate of the much more probable background reactions which can occur while allowing the readout of the tracking information for most of the $pp \rightarrow pp(p\bar{p})$ reactions of interest. This is accomplished using stereo planes of scintillator strips positioned immediately downstream of the last tracking detector. A minimum of two planes (labeled u,v) are required with dip angles of ±45°. The transverse dimensions of the trigger detectors are given in Table 2.

IV.C.1 Trigger inefficiency

The simplest trigger for the experiment corresponds to the condition of observing three protons on the right arm and the anti-proton on the left arm. This condition can be imposed by the trigger: $[(n_{u,left}=1)\bullet(n_{v,left}=1)] \bullet [(n_{u,right}=3)\bullet(n_{v,right}=3)]$. The $n_{i,j}$ refer to the total number of scintillator elements fired for plane i (stereo planes u,v) and detector arm j (*left* or *right*). The trigger is made extremely selective by including in the coincidence only those elements that are expected to be illuminated by the $pp(p\bar{p})$ final state particles at a given ε. This trigger is too restrictive, producing ε-dependent losses when multiple tracks intercept the same trigger element for the $pp(p\bar{p})$ final state. Those losses are shown as a function of ε for different widths of the trigger detector element in Fig. IV.4. Particularly at low ε, there are

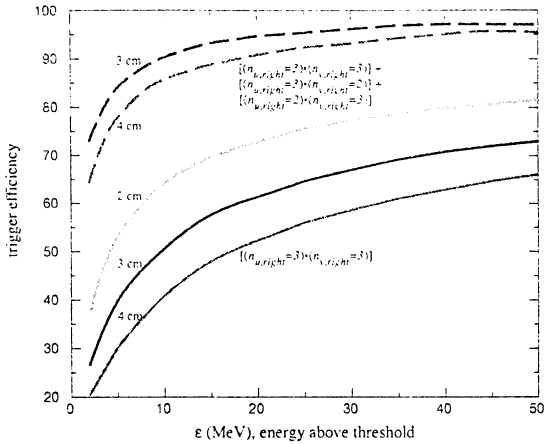

Figure IV.4 Trigger efficiency for the $pp(p\bar{p})$ final state vs. ε for different scintillator hodoscope detector widths.

unacceptably high losses. An alternative is to relax the hit requirement, particularly on the right arm used to detect the three protons. Simply requiring one less hit on the right arm provides trigger efficiencies ≥90% for an acceptable trigger detector element width.

IV.C.2 Sources of background

Table 3 lists the background reactions that are expected to be most problematic. Where measurements exist, cross sections for these processes are included. Otherwise, phase space calculations, normalized to existing measurements, are used to estimate the channel's cross section. Strangeness production channels, such as for pKY and ppK^+K^- final states, do not cause significant backgrounds because of their small production cross sections.

Table 3 Expected dominant sources of background processes, total cross sections and computed trigger rates.

	Final State	σ_{tot} (mb)	Rate (Hz)
Two-prong*			
1.	pp	10	*
2.	$pp+m\pi^0$ with $m\geq1$	~6	*
3.	$pn\pi^++m\pi^0$ with $m\geq0$	~6	*
4.	$nn\pi^+\pi^++m\pi^0$ with $m\geq0$	~6	*
Four-prong (non-strange) from Ref [10]			
5.	$pp\pi^+\pi^-+m\pi^0$ with $m\geq0$	3.0 (m=0)	40
		2.6 (m=1)	30
		0.4 (m=2)	8
6.	$pn\pi^+\pi^+\pi^-+m\pi^0$ with $m\geq0$	~3	35
7.	$nn\pi^+\pi^+\pi^+\pi^-+m\pi^0$ with $m\geq0$	~1	10

* Two-prong channels produce triggers only through pileup, accidental coincidences, secondary interactions of the particles with the magnet poletips, etc.

The final states listed in Table 3 can also be reached through intermediate states involving either baryon or meson resonances. In addition to the backgrounds arising from interactions with the liquid hydrogen target, there are also backgrounds arising from

- beam interactions with the target windows. These backgrounds can be reduced by minimizing the ratio of window to liquid hydrogen scattering centers.
- pileup: at a luminosity of ~3×10^{31} $cm^{-2}s^{-1}$, corresponding to 10^8 protons/sec incident on a 6-cm long liquid hydrogen target, the interaction rate is ~1 MHz. This rate should pose no problem for the trigger, and is comparable to that used in LNS-E213 [8] where pileup has been observed to be negligible. Care must be taken to construct the gas-filled tracking detectors with small enough pitch to make them capable of dealing with high rates. Otherwise, reconstruction errors from extra hits could become a dominant source of background.

The trigger rate for the reactions listed in Table 3 have been estimated via Monte Carlo using the 'loose trigger' requirement and 3 cm wide hodoscope elements. The rates are computed from the known cross sections and the projected luminosity. The size of the trigger region on *det 2* corresponds to the expected image on the detector for ε=50 MeV. At smaller ε, the trigger rates from these background reactions are smaller because of the reduction of the momentum range and maximum angles for the $pp(p\bar{p})$ final state thereby allowing fewer of the scintillator hodoscope elements to be used for the 3 positive + 1 negative particle trigger requirement. At ε=50 MeV, a total trigger rate of 0.5 kHz can be expected. This rate is to be compared to the $pp(p\bar{p})$ yield of ~7 per hour, based on the cross section, luminosity and beam availability estimates given in Sec. III.C. Although highly effective, the trigger is far from sufficient from distinguishing the signal from background. That distinction has to be made using the tracking data and is discussed in the next section.

IV.D Event reconstructions

To determine whether a particular setup leads to a feasible experiment and to establish what level of particle identification is necessary, it is essential to have the rudiments of an event reconstruction code to evaluate simulation results. This section describes the methodology used in the event reconstructions and provides some results for $pp(p\bar{p})$ final state and the reduction of background from other final states.

V.D.1 Methodology

It is assumed that the tracking chambers will properly return the coordinates of a track crossing on one of the detectors and that these coordinates can be properly sorted into tracks. This problem has been treated in some detail in the DISTO [8] reconstruction software which faces the same problem of a complete track reconstruction for 3 positive and 1 negative charged particles and, hence, should not pose a substantially more difficult task for this experiment. The task then, is to take the sorted coordinates from n tracks and

- identify their common vertex, assumed to lie along the beam path
- reconstruct the particle's charge and vector momentum at the vertex.
- distinguish valid $pp(p\bar{p})$ events from background

The first two of these steps are linked to each other: a third spatial coordinate is required for each track to fit the helical trajectory through the magnetic field. That point must come from the reaction vertex. Using these three spatial coordinates, the helical trajectory through the

magnetic field can be fit using the CERNLIB routine MOMENTM. The routine returns the goodness of fit parameter for each track (χ_i^2), the sign of the charge of the particle producing

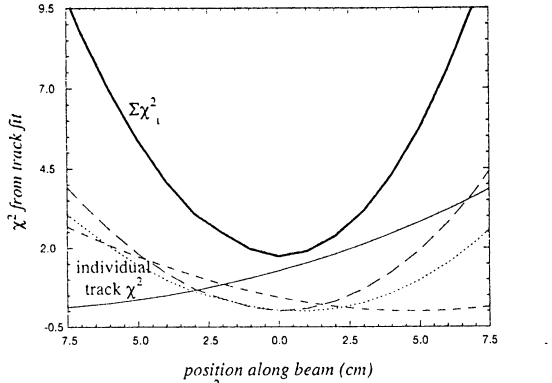

Figure IV.5 The individual track χ_i^2 (returned from MOMENTM) and summed χ_i^2 as a function of the input variable z for the common vertex.

the track, and the vector momentum at the (input) vertex. The best choice for the z-coordinate of the common vertex is when

$$\left.\frac{\partial f}{\partial z}\right|_{z_{vertex}} = 0 \quad \text{where } f(z) = \sum \chi_i^2$$

The functions $f(z)$ and χ_i^2 are shown for a typical event in Fig. IV.5. The curvature of χ_i^2 for an individual track is proportional to p_y for that track. The minimum of χ_i^2 is in general offset from the true vertex because of measurement errors. The assumption that the vertex can be reconstructed by minimizing $f(z)$ is equivalent to assuming that the measurement errors are randomly distributed. The common vertex hypothesis can be tested by examining the value of $f(z_{vertex})$.

V.D.2 Results

The accuracy of the vertex reconstruction is illustrated in Fig. IV.6. The vertex reconstruction error is proportional to the transverse position resolution of the tracking detectors. Worsening the position resolution by a factor of two causes a 50% increase in the sigma of the reconstructed vertex distribution. Due to the fact that the vertex is included in the helical trajectory track fit, the vector momentum sum, $\mathbf{P}_{sum} = \sum \mathbf{p}_i$, is correlated with the deduced vertex. In principle, this could be used to improve the accuracy of the vertex determination. In practice, $\mathbf{P}_{sum}$ is an important distinction between signal and background (especially for final states where there are unobserved particles), hence imposing the condition $\mathbf{P}_{sum}$=0 to determine the vertex could compromise the integrity of this cut.

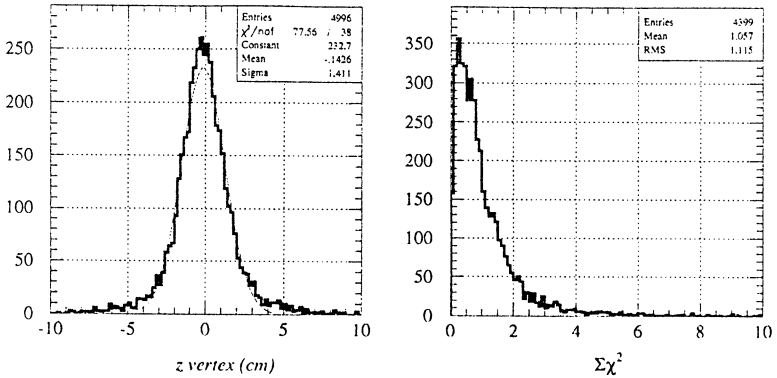

Figure IV.6 Distribution of vertex reconstruction errors and the summed χ^2 in the reconstruction of $pp(p\bar{p})$ final states.

The magnitude of the individual momenta are determined to better than 1% using either straw-tube or MWDC tracking detectors, as illustrated in Fig. IV.7. This accuracy is artificially high since no measurement error is included in the magnetic field: the identical magnetic field map is used in both the simulations and the reconstructions. In practice, magnetic field map errors and/or non-uniformities in the magnetic field will manifest themselves by worsening the momentum resolution. Furthermore, errors associated with recovering spatial coordinates from the hit information of the tracking detector as well as track sorting errors will all go in the direction of deteriorating the momentum resolution. In the simulations that have been performed, comparable momentum reconstruction errors are observed for all 4-charged-particle final states.

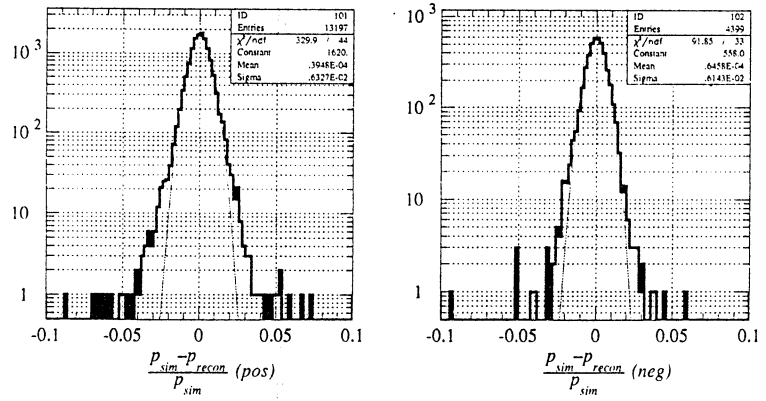

Figure: IV.7 Distribution of the relative momentum magnitude error for positive and negative tracks in the reconstruction of $pp(p\bar{p})$ final states.

The resolution in the components of $\mathbf{P}_{sum}$ and in the squared missing mass with the hypothesis of $pp(p\bar{p})$ final states is crucial for kinematic distinctions between signal and background. Fig. IV.8 shows these quantities, along with the gates used to establish the validity of the final-state particle hypothesis. As illustrated, the gates used are quite loose. This is to account for the many different mechanisms that will worsen the resolution in the kinematic reconstructions compared to what is present in the simulations.

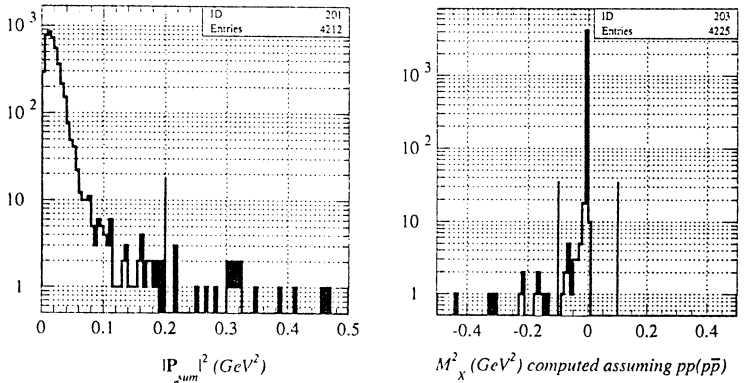

Figure: IV.8 $|\mathbf{P}_{sum}|^2$ and M^2 determined from the reconstruction of $pp(p\bar{p})$ final states.

V.D.3 Backgrounds

The ultimate success or failure of the experiment will be its ability to reduce the effective background cross section to values below that expected for the $pp(p\bar{p})$ final state. This background reduction can be accomplished via kinematic cuts and/or explicit particle identification. Since the kinematic information requires the basic tracking elements already discussed, it is natural to see the degree of background reduction using only the tracking measurements. There are three essential conditions that an event must satisfy to be a candidate $pp(p\bar{p})$ event:

- all components of $\mathbf{P}_{sum}$ must be zero. This condition is imposed by demanding $|\mathbf{P}_{sum}|^2 \leq 0.2\ \mathrm{GeV}^2/c^2$.
- the squared missing mass computed assuming a $pp(p\bar{p})$ final state must be zero. The condition $|M^2| \leq 0.1\ \mathrm{GeV}^2$ is used.
- Individual particles must have their CM momentum satisfy $p_{CM} \leq p_{max} + \delta p$, where δp is chosen to account for finite resolution. In practice, this condition is imposed by computing the total energy in the CM assuming a $pp(p\bar{p})$ final state.

Reconstruction of $pp\pi^+\pi^-\pi^0$ final state for events that satisfy the level-1 trigger and all cuts applied to $pp(p\bar{p})$. Events are distributed according to phase space at ε=50 MeV.

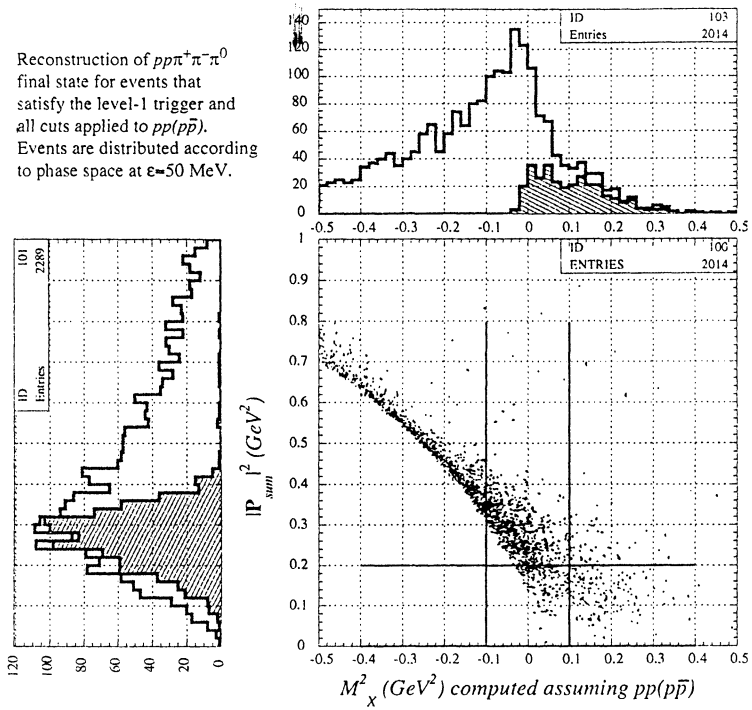

Figure: IV.9 Correlation between $|\mathbf{P}_{sum}|^2$ and M^2 determined from the reconstruction of $pp\pi^+\pi^-\pi^0$ final states. The hatched projections satisfy the condition imposed on the other variable. The box is the expected location for $pp(p\bar{p})$ events.

Fig. IV.9 shows the correlation between M^2 and $|\mathbf{P}_{sum}|^2$ (and their projections) without the condition on p_{CM} for the individual charged particles for the final state $pp\pi^+\pi^-\pi^0$ with the $\pi^+\pi^-$ incorrectly identified as $p\bar{p}$. This particular channel is the most troublesome, with the most intense population of the M^2 *vs.* $|\mathbf{P}_{sum}|^2$ plane satisfying the conditions expected for $pp(p\bar{p})$ final states. The remaining background from the $pp\pi^+\pi^-\pi^0$ final state and other multi-pion production channels can be almost completely eliminated by imposing the last kinematic condition: namely, all four particles must have their CM momentum smaller than p_{max}. This condition is most readily displayed by computing the total energy, computed assuming a $pp(p\bar{p})$ final state, in the CM. As shown in Fig. IV.10, the $pp(p\bar{p})$ final state has a narrow peak centered at $\sqrt{s}$ of finite width determined by the reconstruction resolution. Other final states will have a broad distribution.

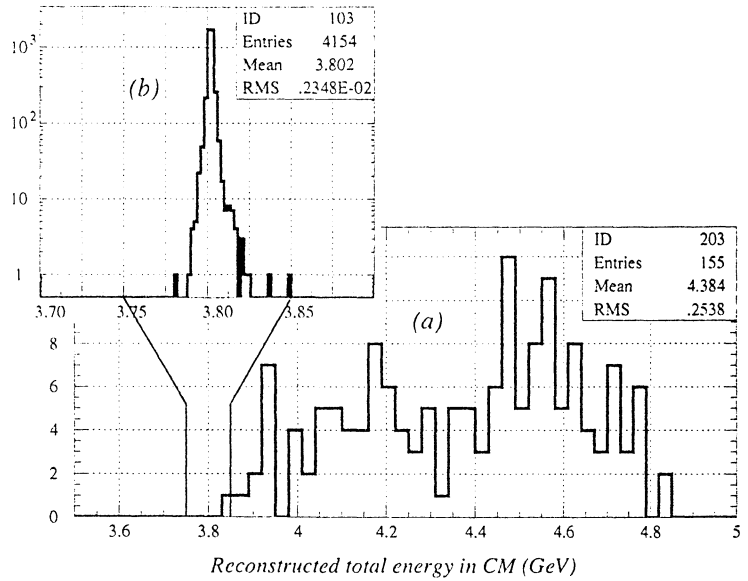

Figure: IV.10 Distribution of the CM summed energy computed from the reconstructed tracks. Figure *(a)* is for the $pp\pi^+\pi^-\pi^0$ final state, with the reconstructed π^+ and π^- incorrectly identified as a proton and anti-proton. Figure *(b)* is for the $pp(p\bar{p})$ final state

The end result is that the effective cross section for misidentifying $pp\pi^+\pi^-\pi^0$ as $pp(p\bar{p})$ is significantly less than 1 nb, the exact value depending on the actual detector resolution. Hence, the theoretically predicted total cross section for the $pp \rightarrow pp(p\bar{p})$ reaction at ε~50 MeV (σ_{tot}~1 nb) should be readily distinguished from background. As indicated in the earlier discussion, only very loose cuts have been employed with the expectation that the final resolution will be worse than what is observed in this simulation. Additional discrimination between pions and protons is provided by the energy deposition in the scintillator hodoscope, as has been demonstrated for comparable momentum particles in LNS-E213 [8]. Backgrounds from other non-strange channels are observed in the simulations to be smaller than for $pp\pi^+\pi^-\pi^0$.

V. Summary

This letter of intent presents the plans for a new experiment for the CERN-PS east hall to measure the total cross section for the near-threshold production of $p\bar{p}$ pairs in pp collisions. The detector apparatus would be a magnetic spectrometer equipped with tracking detectors and a scintillator hodoscope, possibly supplemented with water Çerenkov detectors for additional particle identification information. The detector would have 100% acceptance for all final-state particles in the $pp \rightarrow pp(p\bar{p})$ reaction.

We require the following items from CERN to carry out the experiment in the CERN-PS east hall

- two weeks of a low-energy, low intensity slow extracted proton beam from the CERN-PS at three momenta of 6.54, 6.60 and 6.70 GeV/c to allow measurements at $\varepsilon \equiv \sqrt{s} - 4m_p = 10$, 25 and 50 MeV.
- access to an experimental area in the east hall with a beam line from the CERN-PS. There should be adequate space, electrical power and cooling for a large dipole magnet and a vacuum system intended to encompass the beam, target and magnetic field regions. The simulations presented above assume a 1.5 T magnet covering an area of $(1.3\ \mathrm{m})^2$ with a usable gap between the pole tips of 0.5 m.
- space and power for two symmetric detector arms. A schematic of the apparatus is shown in Fig. III.1
- a beam dump for the primary beam positioned downstream of the detector apparatus.

The other components of the experiment would be provided by the collaboration and would include

- a 6-cm long liquid hydrogen target mounted upstream of the magnet.
- two detector arms immediately downstream of the magnet. Each arm is intended to be contained within a vacuum system and would consist of two stacks of straw-tube detectors for tracking and a scintillator hodoscope.

Final design of the experiment must await the location of a suitable magnet.

VI. Extensions of the apparatus

Although a measurement of the $pp \rightarrow pp(p\bar{p})$ reaction, alone, would be of interest, a program of measurements of the more general $pp \rightarrow ppB\bar{B}$ reaction, would allow intercomparisons of $p\bar{p}$, $n\bar{n}$ and $\Lambda\bar{\Lambda}$ production, hence providing complementary knowledge of the $u\bar{u}$, $d\bar{d}$ and $s\bar{s}$ content of the quark sea to that obtained from meson production. To carry out such a program, extensions of the basic apparatus shown in Fig. III.1 would be required. The simplest extension would be the study of $n\bar{n}$ production. Here, a set of neutron and anti-neutron counters would be placed downstream of the magnet positioned at an angle of 0° with respect to the incoming beam. Counters similar to those used in the PS-199 LEAR experiment [11] would be appropriate. At an even later stage, extensions of the tracking detectors could allow the measurement of $\Lambda\bar{\Lambda}$ production close to its threshold of 7.999 GeV/c. Those measurements would require the detection and triggering on the delayed decays of the $\Lambda\bar{\Lambda}$ pair, using techniques similar to the PS-185 LEAR experiment.

References

[1] M.A. Alberg, E.M. Henley, L. Wilets and P.D. Kunz, Phys. At. Nucl. **57**, 1608 (1994).

[2] T.S. Lee and D.O. Riska, Phys. Rev. Let. **70** (1993) 2237; C.J. Horowitz, et al. Phys. Rev. C **49** (1994) 1337.

[3] K. Kilian and H. Nann, AIP Conf. Proc. 221 (1990) 185.

[4] G.I. Lykasov, M.V. Rzjanin and W. Cassing, Phys Lett. **B387** (1996) 691

[5] *Light-Ion Spin Synchrotron*, IUCF internal report (1996).

[6] P. Danielewicz, Phys. Rev. C **42**, 1564 (1990).

[7] B. Nilsson-Almqvist and E. Stenlund, Comp. Phys. Comm. **43**, 387 (1987).

[8] R. Bertini, *et al.* "Strangeness Production in the p-N and p-Nucleus Interaction", LNS-E213 proposal (1996).

[9] H.A. Enge, Rev. Sci. Instr. **35**, 278 (1964).

[10] G. Yekutieli, et al., Nucl. Phys. **B18**, 301 (1970).

[11] R. Birsa, et al., Nucl. Phys. **B403**, 25 (1993).